

Enhanced optical nonlinearity and fiber-optical frequency comb controlled by a single atom in a whispering-gallery-mode microtoroid resonator

Jiahua Li,^{1,2} Suzhen Zhang,¹ Rong Yu,^{3,*} Duo Zhang,⁴ and Ying Wu^{1,†}

¹*School of Physics, Huazhong University of Science and Technology, Wuhan 430074, People's Republic of China*

²*Key Laboratory of Fundamental Physical Quantities Measurement of Ministry of Education, Wuhan 430074, People's Republic of China*

³*School of Science, Hubei Province Key Laboratory of Intelligent Robot, Wuhan Institute of Technology, Wuhan 430073, People's Republic of China*

⁴*School of Electrical and Electronic Engineering, Wuhan Polytechnic University, Wuhan 430023, People's Republic of China*

(Received 21 September 2014; revised manuscript received 20 October 2014; published 17 November 2014)

Based on a single atom coupled to a fiber-coupled, chip-based microresonator [B. Dayan *et al.*, *Science* **319**, 1062 (2008)], we put forward a scheme to generate optical frequency combs at driving laser powers as low as a few nanowatts. Using state-of-the-art experimental parameters, we investigate in detail the influences of different atomic positions and taper-resonator coupling regimes on optical-frequency-comb generation. In addition to numerical simulations demonstrating this effect, a physical explanation of the underlying mechanism is presented. We find that the combination of the atom and the resonator can induce a large third-order nonlinearity which is significantly stronger than Kerr nonlinearity in Kerr frequency combs. Such enhanced nonlinearity can be used to generate optical frequency combs if driven with two continuous-wave control and probe lasers and significantly reduce the threshold of nonlinear optical processes. The comb spacing can be well tuned by changing the frequency beating between the driving control and probe lasers. The proposed method is versatile and can be adopted to different types of resonators, such as microdisks, microspheres, microtoroids or microrings.

DOI: [10.1103/PhysRevA.90.053832](https://doi.org/10.1103/PhysRevA.90.053832)

PACS number(s): 42.62.Eh, 42.50.Pq, 42.65.Ky, 42.50.Ct

I. INTRODUCTION

On account of both ultrahigh quality factors and very small mode volumes [1], optical microresonators enable greatly enhanced light-matter interactions as well as drastic reductions of the power necessary to observe strong nonlinear optical effects. In the past few years, optical microresonators are increasingly attracting interest in many diverse areas of fundamental researches and applications, including biochemical sensing [2,3], cavity quantum electrodynamics (QED) [4–6], quantum information processing (QIP) [7], cavity optomechanics [8–10], low-threshold microlasers [11–14], optical filtering [15,16], and enhanced Raman gain [17,18], etc. The massive on-chip fabrication and excellent scalability also make them promising for real applications. Optical microresonators support whispering-gallery modes (WGMs). Unlike the standing modes in a conventional Fabry-Pérot microcavity, WGMs are a type of traveling mode. In other words, WGM microresonators typically support two counterpropagating modes, i.e., clockwise (CW) and counterclockwise (CCW) propagating modes, with the same polarization and a degenerate frequency. This degeneracy can be lifted, and it can form a doublet through backscattering coupling induced by internal defect centers or surface roughness [19,20]. This phenomenon is known as modal coupling [21]. Dipole emitters in the vicinity of the resonator are able to interact with the two WGMs via the evanescent field. With the help of the taper fiber, the efficiency for coupling the quantum fields into and out of the microresonator can approach 99%–99.9% [5,22]. A distinctive feature of taper-coupled microresonator is that the coupling strength

can be continuously adjusted by tuning the taper-resonator gap. This allows one to access different coupling regimes [23].

Making good use of the above-mentioned coherent interactions between the microresonators and quantum emitters, some microchip-based schemes about photon turnstiles [24,25], photon routers [26,27], single-photon transistors [28], optical switching [29,30], and quantum controlled-phase-flip gates [31,32] have been put forward theoretically and experimentally. It is worth pointing out that, in the investigation of Ref. [24], Dayan *et al.* have addressed that, with quantum critical coupling of input lights into and out of a microtoroidal resonator, a single cesium atom near the surface of the resonator can dynamically control the cavity output depending on the photon number at the input. Strong coupling between single caesium or rubidium atoms and the electromagnetic mode in a microtoroid has been theoretically investigated and experimentally observed in a few pioneering works [33–35]. In Ref. [33], it is also demonstrated that the caesium atom can transfer its excitation to the CW or CCW mode which is intrinsic in the microtoroidal resonators under a certain condition. In a word, beyond their importance in strong light-matter coupling, WGM microresonators are highly versatile photonic devices that have found applications in a large variety of disciplines.

On the other hand, the introduction of optical frequency combs has led to qualitatively revolutionize the measurement of time and frequency, with previously unattainable precision [36,37]. Optical frequency combs consist of periodic discrete spectral lines with fixed frequency positions and are generally characterized by only two degrees of freedom, its mode spacing and the carrier-envelope offset frequency [38]. The Hänsch group has demonstrated in their early work on femtosecond mode-locked lasers that the periodic pulse train emitted by these devices intrinsically constitutes an optical frequency comb in the spectral domain [39]. During the past few years, a novel type of on-chip comb generator [40–49] has sparked

*Author to whom correspondence should be addressed: yurong321@126.com

†yingwu2@126.com

significant scientific interest in new techniques and expanding applications of optical frequency comb generation. Such new frequency comb generation principle is based on cascaded four-wave mixing (FWM) in compact optical microresonators with Kerr nonlinearity materials and does not utilize conventional stimulated laser emission. However, for achieving the intensity-dependent refractive index (or the $\chi^{(3)}$ Kerr nonlinearity), optical-frequency-comb generation in each of these ultra-high- Q microresonators platforms requires tuning a high-power, single-frequency (monochromatic), continuous-wave pump laser into a resonance of the monolithic high- Q microresonator, where a third-order nonlinearity material is embedded [41].

Based on these achieved advances, in the present work we discuss the use of a tapered-fiber-coupled microtoroidal WGM resonator together with a single cesium atom to generate a type of optical frequency microcomb with low-power optical input. The optical modes of the microtoroidal resonator are coherently excited by the external lasers through the tapered fiber. Beyond the weak-excitation approximation, our results show that the combination of the atom and the resonator induces a large nonlinearity which is significantly stronger than Kerr nonlinearity [41] and significantly reduces the threshold of nonlinear optical processes. This nonlinearity can be used to generate optical frequency combs if driven with two continuous-wave control and probe lasers, where the comb spacing is given by the frequency beating between the driving control and probe lasers. The main advantages of applying our considered atom-resonator-fiber QED scheme over other approaches are as follows:

(i) The small confinement volume, high photon density, and long photon storage time in the resonator induce a very strong atom-field interaction and nonlinearity, which lead to a significant reduction in the threshold of nonlinear optical processes. So, an important property of this method for optical-frequency-comb generation is very low power consumption (pump power of a few nW), compared with Kerr frequency comb generation (a few hundred mW) [41].

(ii) The comb spacing can be well tuned by changing the frequency beating between the driving control and probe lasers.

(iii) Our generated frequency comb is robust against large variations of atomic position and coupling regime.

II. MODEL, HAMILTONIAN, AND HEISENBERG-LANGEVIN EQUATIONS

Figure 1 is a schematic description of the composite system, which consists of a microtoroidal resonator, a tapered fiber, and a two-level caesium atom. A microtoroidal resonator has two internal counterpropagating modes which are described in terms of the annihilation (creation) operators \hat{a} (\hat{a}^\dagger) and \hat{b} (\hat{b}^\dagger) with a common frequency ω_R in the absence of scattering. These two modes are coupled to each other in the presence of scattering off imperfections with a strength that is parametrized by h . The total decay of the resonator field (the resonator linewidth) is denoted by a rate $\kappa = \kappa_i + \kappa_{ex}$, where κ_i is the resonator intrinsic decay rate, related to the intrinsic quality factors Q_i as $\kappa_i = \omega_R/2Q_i$ and κ_{ex} is the external loss rate (i.e., fiber taper-resonator coupling), related to the coupling

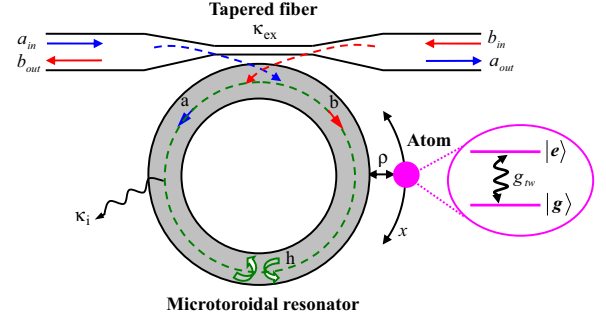


FIG. 1. (Color online) Schematics of the system. A two-level atom (orange sphere) is coupled to a microtoroidal resonator (gray toroid) which is side-coupled to a single-mode tapered fiber (white taper). The two degenerate whispering-gallery modes are labeled a (counterclockwise) and b (clockwise), respectively. The coupling between the atom and each WGM is g_{tw} . Input to and output from the internal modes of the resonator are provided by a tapered fiber. The coupling strength of each WGM to the tapered fiber is κ_{ex} . The strength of the intermode scattering between two WGM's is h . The intrinsic loss of the atom and of each WGM is γ and κ_i , respectively. The external input and output fields are described by the symbols $\{a_{in}, a_{out}, b_{in}, b_{out}\}$, respectively.

quality factor Q_{ex} as $\kappa_{ex} = \omega_R/2Q_{ex}$. The intracavity fields are coupled to a tapered fiber with high efficiency [5,22]. At the same time, the resonator evanescent fields of modes \hat{a} and \hat{b} have the coherent interactions with a ground state $|g\rangle$ and an upper excited state $|e\rangle$ (atomic transition frequency ω_A) of a two-level atom near the external surface of the microtoroidal resonator. The atomic spontaneous emission decay rate is γ . Using the tapered fiber coupler [22], an initial two-tone continuous-wave driving field, denoted by $a_{in}(t) = \mathcal{E}_c e^{-i\omega_c t} + \mathcal{E}_p e^{-i\omega_p t}$ with the field strengths (carrier frequencies) \mathcal{E}_c and \mathcal{E}_p (ω_c and ω_p), is guided by the fiber waveguide to only drive the resonator mode \hat{a} . The input field to mode \hat{b} is taken to be vacuum. Details of the device design have been previously reported [24,33,50,51]. In a frame rotating at the control frequency ω_c , the Hamiltonian for the system can be written in the form (setting $\hbar = 1$) [50,51],

$$\begin{aligned} \hat{H} = & \Delta_A \hat{\sigma}_{ee} + \Delta_R (\hat{a}^\dagger \hat{a} + \hat{b}^\dagger \hat{b}) + h (\hat{a} \hat{b}^\dagger + \hat{a}^\dagger \hat{b}) \\ & + (g_{tw} \hat{a} \hat{\sigma}_{eg} + g_{tw}^* \hat{a}^\dagger \hat{\sigma}_{ge}) + (g_{tw} \hat{b} \hat{\sigma}_{eg} + g_{tw}^* \hat{b}^\dagger \hat{\sigma}_{ge}) \\ & + i\sqrt{2\kappa_{ex}} [(\mathcal{E}_c + \mathcal{E}_p e^{-i\Omega t}) \hat{a}^\dagger - (\mathcal{E}_c^* + \mathcal{E}_p^* e^{i\Omega t}) \hat{a}], \quad (1) \end{aligned}$$

where $\Delta_A = \omega_A - \omega_c$, $\Delta_R = \omega_R - \omega_c$, and $\Omega = \omega_p - \omega_c$ are, respectively, the detunings of the transition frequency of the two-level atom ω_A , the “bare” resonator mode frequency ω_R , and the probe laser frequency ω_p from the control laser frequency ω_c . The coherent interaction of the two-level atom with the evanescent traveling-wave fields of the intracavity modes \hat{a} , \hat{b} is described by $g_{tw} = g_0^{tw} f(\rho, z) e^{\pm ikx}$, where ρ is the radial distance of the atom from the surface of the toroid, x is the atom's position around the circumference of the toroid, and z is the vertical coordinate along the symmetry axis. k is the vacuum wave vector. The \pm refers to the clockwise or counterclockwise propagating mode. $\hat{\sigma}_{ge}$ ($\hat{\sigma}_{eg}$) is the lowering (raising) operator and $\hat{\sigma}_{ee}$ is the population operator for the atom. The field strengths $\mathcal{E}_{c,p}$ are normalized to a photon flux

at the input of the cavity and directly related to the power propagating in the tapered fiber by $P_{c,p} = \hbar\omega_{c,p}\mathcal{E}_{c,p}^2$.

The Hamiltonian and Heisenberg-Langevin equations of motion for the coupled atom-resonator system can also be usefully expressed in terms of the normal modes of the microtoroidal resonator. Following the method developed in Refs. [50,51], transforming traveling to standing modes $\hat{A} = (\hat{a} + \hat{b})/\sqrt{2}$ and $\hat{B} = (\hat{a} - \hat{b})/\sqrt{2}$, the Hamiltonian can be written as

$$\begin{aligned} \hat{\mathcal{H}} = & \Delta_A \hat{\sigma}_{ee} + (\Delta_R + h)\hat{A}^\dagger \hat{A} + (\Delta_R - h)\hat{B}^\dagger \hat{B} \\ & + g_A(\hat{A}^\dagger \hat{\sigma}_{ge} + \hat{A} \hat{\sigma}_{eg}) - i g_B(\hat{B}^\dagger \hat{\sigma}_{ge} - \hat{B} \hat{\sigma}_{eg}) \\ & + i\sqrt{\kappa_{ex}}[(\mathcal{E}_c + \mathcal{E}_p e^{-i\Omega t})\hat{A}^\dagger - (\mathcal{E}_c^* + \mathcal{E}_p^* e^{i\Omega t})\hat{A}] \\ & + i\sqrt{\kappa_{ex}}[(\mathcal{E}_c + \mathcal{E}_p e^{-i\Omega t})\hat{B}^\dagger - (\mathcal{E}_c^* + \mathcal{E}_p^* e^{i\Omega t})\hat{B}], \end{aligned} \quad (2)$$

where $g_A = \sqrt{2}\text{Re}(g_{tw}) = g_0 f(\rho, z) \cos(kx)$, $g_B = \sqrt{2}\text{Im}(g_{tw}) = g_0 f(\rho, z) \sin(kx)$, and $g_0 = \sqrt{2}g_0^{tw}$. One can find that, depending on the position of the atom, the coherent coupling can occur predominantly (or even exclusively) to only one of the two normal modes. For $kx = n\pi$ (n is an integer), the atom couples only to mode \hat{A} of frequency $\omega_R + h$ with strength g_0 , while for $kx = n\pi + \pi/2$, the atom couples only to mode \hat{B} of frequency $\omega_R - h$ with strength g_0 . For $kx = n\pi + \pi/4$, the atom couples simultaneously to two normal modes \hat{A} and \hat{B} .

According to the above Hamiltonian (2), the quantum Heisenberg-Langevin equations of motion for the coupled system are given by

$$\begin{aligned} \frac{d\hat{A}}{dt} = & -[i(\Delta_R + h) + \kappa_i/2 + \kappa_{ex}/2]\hat{A} - i g_A \hat{\sigma}_{ge} \\ & + \sqrt{\kappa_{ex}}(\mathcal{E}_c + \mathcal{E}_p e^{-i\Omega t}) + \hat{f}_A, \end{aligned} \quad (3)$$

$$\begin{aligned} \frac{d\hat{B}}{dt} = & -[i(\Delta_R - h) + \kappa_i/2 + \kappa_{ex}/2]\hat{B} - g_B \hat{\sigma}_{ge} \\ & + \sqrt{\kappa_{ex}}(\mathcal{E}_c + \mathcal{E}_p e^{-i\Omega t}) + \hat{f}_B, \end{aligned} \quad (4)$$

$$\begin{aligned} \frac{d\hat{\sigma}_{gg}}{dt} = & \gamma \hat{\sigma}_{ee} - i g_A \hat{A}^\dagger \hat{\sigma}_{ge} + i g_A \hat{A} \hat{\sigma}_{eg} \\ & - g_B \hat{B}^\dagger \hat{\sigma}_{ge} - g_B \hat{B} \hat{\sigma}_{eg} + \hat{f}_{gg}, \end{aligned} \quad (5)$$

$$\begin{aligned} \frac{d\hat{\sigma}_{ee}}{dt} = & -\gamma \hat{\sigma}_{ee} + i g_A \hat{A}^\dagger \hat{\sigma}_{ge} - i g_A \hat{A} \hat{\sigma}_{eg} \\ & + g_B \hat{B}^\dagger \hat{\sigma}_{ge} + g_B \hat{B} \hat{\sigma}_{eg} + \hat{f}_{ee}, \end{aligned} \quad (6)$$

$$\begin{aligned} \frac{d\hat{\sigma}_{ge}}{dt} = & -(i\Delta_A + \gamma/2)\hat{\sigma}_{ge} - i g_A \hat{A}(\hat{\sigma}_{gg} - \hat{\sigma}_{ee}) \\ & + g_B \hat{B}(\hat{\sigma}_{gg} - \hat{\sigma}_{ee}) + \hat{f}_{ge}, \end{aligned} \quad (7)$$

where Eqs. (3) and (4) describe the dynamics of the resonator modes. Equations (5)–(7) describe the dynamics of the two-level atom. The operators \hat{f}_A , \hat{f}_B , \hat{f}_{gg} , \hat{f}_{ee} , and \hat{f}_{ge} are the noise operators that conserve the commutation relations at all times.

The interactions between a high-Q microresonator and a single atom (or a solid-state quantum emitter) have been intensively studied previously with the weak-excitation regime

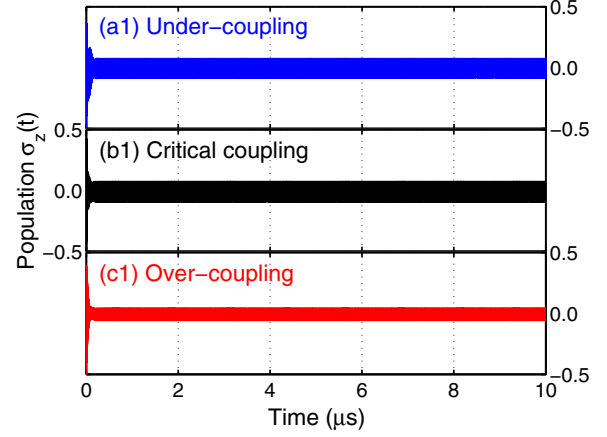


FIG. 2. (Color online) Evolution of atomic population $\sigma_z(t)$ as a function of time t for three different resonator coupling regimes, namely, (a) undercoupling $\{\kappa_{ex}, \kappa_i, h\}/2\pi = \{5, 75, 50\}$ MHz, (b) critical coupling $\{\kappa_{ex}, \kappa_i, h\}/2\pi = \{90, 75, 50\}$ MHz, and (c) overcoupling $\{\kappa_{ex}, \kappa_i, h\}/2\pi = \{300, 75, 50\}$ MHz. The other system parameters used for the simulations are as follows: atom-resonator interaction strength $g_0/2\pi = 70$ MHz, driving laser strengths $\mathcal{E}_c = \mathcal{E}_p = 100 \text{ MHz}^{1/2}$ ($P_c = P_p = 84 \text{ nW}$), relative detunings $\Delta_A/2\pi = \Delta_R/2\pi = 0$, $\Omega/2\pi = 50$ MHz, atomic spontaneous emission rate $\gamma/2\pi = 5.2$ MHz, and azimuthal position of the atom $kx = 0$, respectively. The above given system parameters for the microtoroidal resonator, fiber taper, and cesium atom are based on Refs. [24,26,33].

[24–33,52–56]. In the general case, the above Heisenberg-Langevin equations are difficult to analytically solve as they are not in a closed form and thus form an infinite hierarchy of equations. For many problems, the weak-excitation approximation was adopted to simplify these equations [50,51], where all the electrons are predominantly in the ground state of the two-level atom, i.e., $\hat{\sigma}_{gg}(t) = 1$ and $\hat{\sigma}_{ee}(t) = 0$, or $\hat{\sigma}_z(t) = (\hat{\sigma}_{ee}(t) - \hat{\sigma}_{gg}(t))/2 = -1/2$. By assuming this so-called weak-excitation approximation, one can substitute $\hat{\sigma}_{gg}(t)$, $\hat{\sigma}_{ee}(t)$, or $\hat{\sigma}_z(t)$ with its average value of 1, 0, or $-1/2$ for all time, and thus linearize the Heisenberg-Langevin equations. It should be pointed out that, beyond the weak-excitation approximation, some obvious nonlinear effects may occur. Figures 2 and 3,

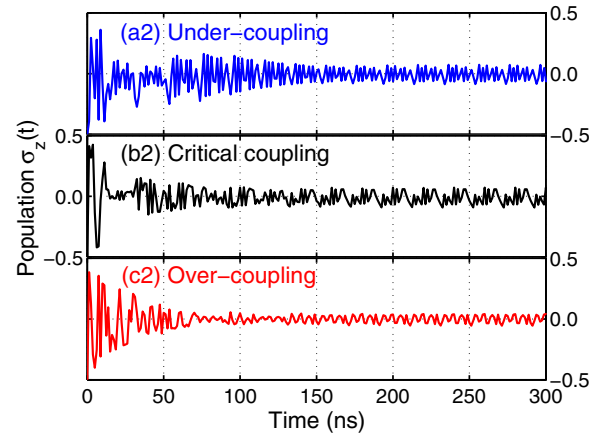


FIG. 3. (Color online) A magnified view of Fig. 2 in a short time.

on one hand, show that the weak-excitation approximation is invalid for the system parameters considered here because of $\sigma_z(t) \neq -1/2$ for all time. On the other hand, it can be seen from Figs. 2 and 3 that the atom saturation [i.e., $\sigma_z(t) = 0$ for all time] is absent for the chosen power of the driving laser. The atom saturates with increasing power of the driving laser. To this end, we need to take into account the nonlinear nature of the atom-resonator coupling, i.e., all the higher-order moments $i g_A \hat{A} \hat{\sigma}_{eg}$, $-g_B \hat{B} \hat{\sigma}_{eg}$, $-i g_A \hat{A} (\hat{\sigma}_{gg} - \hat{\sigma}_{ee})$, and $g_B \hat{B} (\hat{\sigma}_{gg} - \hat{\sigma}_{ee})$ in Eqs. (5)–(7). Recently, it has been demonstrated that these nonlinear terms can give rise to some interesting phenomena of the coupled emitter-cavity system, such as nonlinear optical spectroscopy [57,58], nanophotonic comb creation [59], all-optical latching and modulation [60], optical chaos [61], ultralow power and high-speed all-optical switching [62], and so on.

Experimentally, the parameter κ_{ex} can be continuously adjusted by setting the resonator-fiber distances using a piezo positioning system. The relative values of κ_{ex} , κ_i , and h determine the resonator coupling regime [24,30]: (i) $\kappa_{ex} < \kappa_i$ and h , the losses predominate and the resonator is under-coupled. (ii) $\kappa_{ex} = \sqrt{\kappa_i^2 + h^2}$; the resonator is critically coupled. (iii) $\kappa_{ex} > \kappa_i$ and h ; the resonator is overcoupled. The output field can be obtained by $a_{\text{out}} = -a_{\text{in}} + \sqrt{\kappa_{ex}}(\hat{A} + \hat{B})$ and $b_{\text{out}} = -b_{\text{in}} + \sqrt{\kappa_{ex}}(\hat{A} - \hat{B})$ [30,50,51]. In what follows, we calculate the output power spectra $S_a(\omega)$ and $S_b(\omega)$ of the system given by $S_a(\omega) = \int_{-\infty}^{\infty} \kappa_{ex} \langle \hat{a}_{\text{out}}^\dagger(t) \hat{a}_{\text{out}}(t) \rangle e^{-i\omega t} dt$ and $S_b(\omega) = \int_{-\infty}^{\infty} \kappa_{ex} \langle \hat{b}_{\text{out}}^\dagger(t) \hat{b}_{\text{out}}(t) \rangle e^{-i\omega t} dt$, where ω is the spectrometer frequency. Before passing to the results of the numerical calculation, it should be noted that the spectra obtained shift a frequency ω_c , because the Heisenberg-Langevin equations describe the evolution of the optical field in a frame rotating at the control frequency ω_c . In this paper, we are interested in the mean response of the system, so we consider their expectation values of both sides of Eqs. (3)–(7). We take the cold reservoir limit where the reservoir modes are all initially in the vacuum states. In this limit, the reservoirs act only to draw away energy and do not excite the system by means of thermal excitations. For optical frequencies and temperatures at or below room temperature, this assumption holds very well [25,63]. When acting on the initial vacuum state, in the cold reservoir limit the expectation values of all noise operators can be neglected because they are annihilated. In this scenario, we reduce the operator equations to the mean value equations and drop the above quantum noise terms because of $\langle \hat{f}_A \rangle = 0$, $\langle \hat{f}_B \rangle = 0$, $\langle \hat{f}_{gg} \rangle = 0$, $\langle \hat{f}_{ee} \rangle = 0$, and $\langle \hat{f}_{ge} \rangle = 0$.

III. ATOM-RESONATOR-INDUCED STRONG NONLINEARITY AND EFFICIENT OPTICAL-FREQUENCY-COMB GENERATION

A. Atom-resonator-induced nonlinearity

In order to explicitly get insight into the atom-resonator-induced nonlinearity under the steady-state solution, here we consider the case that the driving laser field is monochromatic by setting $\mathcal{E}_p = 0$, i.e., the probe driving field is switched off. The Heisenberg-Langevin equations then

become

$$\frac{dA}{dt} = -[i(\Delta_R + h) + \kappa_i/2 + \kappa_{ex}/2]A - i g_A \sigma_{ge} + \sqrt{\kappa_{ex}} \mathcal{E}_c, \quad (8)$$

$$\frac{dB}{dt} = -[i(\Delta_R - h) + \kappa_i/2 + \kappa_{ex}/2]B - g_B \sigma_{ge} + \sqrt{\kappa_{ex}} \mathcal{E}_c, \quad (9)$$

$$\frac{d\sigma_z}{dt} = -\gamma(\sigma_z + 1/2) + i g_A A^* \sigma_{ge} - i g_A A \sigma_{ge}^* + g_B B^* \sigma_{ge} + g_B B \sigma_{ge}^*, \quad (10)$$

$$\frac{d\sigma_{ge}}{dt} = -(i\Delta_A + \gamma/2)\sigma_{ge} + 2i g_A A \sigma_z - 2g_B B \sigma_z, \quad (11)$$

where $\sigma_z = (\sigma_{ee} - \sigma_{gg})/2$ is the population difference between the atomic excited and ground states. The derivation of Eqs. (8)–(11) uses the mean-field (factorization) assumption $\langle \hat{A} \hat{B} \rangle = \langle \hat{A} \rangle \langle \hat{B} \rangle$. In semiclassical formalism the field is a well-defined (i.e., noise free) classical amplitude, thus the expectations of products of a field operator and dipole operator are separable [25,63].

Following standard methods from quantum optics, we will apply a nonlinear perturbation theory to the coupled atom-resonator-fiber system and search for the formation of optical nonlinearity for the propagating field in a tapered fiber. To make the nonlinear effect of the system significant, the power (or intensity) of the driving control laser should be chosen properly to deplete the population σ_{gg} of the ground state $|g\rangle$. We go beyond the linear theory by systematically including the depletion of the ground-state population. We assume that the dispersion and nonlinearity of the system are not strong so that a standard method of multiple scales [64] can be used to derive the nonlinearly coupled transmission coefficients for both resonator modes. For this purpose, we make the following asymptotic expansion:

$$A = \varepsilon A^{(1)} + \varepsilon^2 A^{(2)} + \varepsilon^3 A^{(3)} + \dots + \varepsilon^j A^{(j)} + \dots, \quad (12)$$

$$B = \varepsilon B^{(1)} + \varepsilon^2 B^{(2)} + \varepsilon^3 B^{(3)} + \dots + \varepsilon^j B^{(j)} + \dots, \quad (13)$$

$$\sigma_z = \sigma_z^{(0)} + \varepsilon \sigma_z^{(1)} + \varepsilon^2 \sigma_z^{(2)} + \varepsilon^3 \sigma_z^{(3)} + \dots, \quad (14)$$

$$\sigma_{ge} = \sigma_{ge}^{(0)} + \varepsilon \sigma_{ge}^{(1)} + \varepsilon^2 \sigma_{ge}^{(2)} + \varepsilon^3 \sigma_{ge}^{(3)} + \dots, \quad (15)$$

where ε is a small parameter characterizing the small population depletion in the ground state $|g\rangle$ and ranging from zero to unity. Equations (8)–(11) can be solved order by order by means of the above asymptotic expansion (12)–(15). The case for $j = 1$ is just the linear problem. Initially, the electron in the atom is populated in the ground state $|g\rangle$. In this situation, we have $\sigma_z^{(0)} = -1/2$ and $\sigma_{ge}^{(0)} = 0$ for the zeroth-order electronic operators [65–67]. We substitute the above asymptotic expansion (12)–(15) into Eqs. (8)–(11) and keep the terms up to the third order in the amplitude of the resonator fields. Specifically, we display the three different cases as listed below.

Case (i) $kx = n\pi$ (n is an integer). The atom couples only to mode A . After performing some algebraic calculations, the amplitude of the resonator field A under the steady-state case reads

$$A^{(1)} = \frac{\sqrt{\kappa_{ex}}d_1}{g_A^2 + d_1d_2} \mathcal{E}_c, \quad A^{(2)} = 0, \quad (16)$$

$$A^{(3)} = \frac{2g_A^4\sqrt{\kappa_{ex}}d_1}{\gamma(g_A^2 + d_1d_2)^2} \left(\frac{1}{d_1} + \frac{1}{d_1^*} \right) \left| \frac{\sqrt{\kappa_{ex}}d_1}{g_A^2 + d_1d_2} \right|^2 \mathcal{E}_c |\mathcal{E}_c|^2, \quad (17)$$

with $d_1 = i\Delta_A + \gamma/2$ and $d_2 = i(\Delta_R + h) + \kappa_i/2 + \kappa_{ex}/2$. As a result, the transmission field a_{out} and b_{out} can be obtained by using the input-output relation as follows:

$$\begin{aligned} a_{\text{out}} &= -\mathcal{E}_c + \sqrt{\kappa_{ex}}A^{(1)} + \sqrt{\kappa_{ex}}A^{(3)} \\ &= \chi_a^{(1)}\mathcal{E}_c + \chi^{(3)}|\mathcal{E}_c|^2\mathcal{E}_c, \end{aligned} \quad (18)$$

$$\begin{aligned} b_{\text{out}} &= \sqrt{\kappa_{ex}}A^{(1)} + \sqrt{\kappa_{ex}}A^{(3)} \\ &= \chi_b^{(1)}\mathcal{E}_c + \chi^{(3)}|\mathcal{E}_c|^2\mathcal{E}_c, \end{aligned} \quad (19)$$

with $\chi_a^{(1)} = -1 + \frac{\kappa_{ex}d_1}{g_A^2 + d_1d_2}$, $\chi_b^{(1)} = \frac{\kappa_{ex}d_1}{g_A^2 + d_1d_2}$, and $\chi^{(3)} = \frac{2g_A^4\kappa_{ex}^2d_1}{\gamma(g_A^2 + d_1d_2)^2} \left(\frac{1}{d_1} + \frac{1}{d_1^*} \right) \left| \frac{d_1}{g_A^2 + d_1d_2} \right|^2$.

From the above expressions (18) and (19), it is easy to see that a_{out} and b_{out} are proportional to \mathcal{E}_c and $|\mathcal{E}_c|^2\mathcal{E}_c$, respectively. Therefore, such an expression can be correspondingly made an analogy to the linear and third-order nonlinear polarization [68,69]. The term a_{out} (or b_{out}) exhibits the linear response and the Kerr nonlinear response of the coupled atom-resonator-fiber system to the input signal field. Specifically, $|\chi^{(1)}|^2$ stands for the normalized linear transmission of the atom-resonator-fiber system, while the real part $\text{Re}[\chi^{(3)}]$ corresponds to Kerr nonlinearity and the imaginary part $\text{Im}[\chi^{(3)}]$ corresponds to nonlinear absorption. It is easy to find from Eqs. (18) and (19) that the third-order nonlinear optical effects exist due to the atom-resonator coupling. When $g_A = 0$, we have the result $\chi^{(3)} = 0$.

Case (ii) $kx = n\pi + \pi/2$. The atom couples only to mode B . Similarly, we have the results,

$$B^{(1)} = \frac{\sqrt{\kappa_{ex}}d_1}{g_B^2 + d_1d_3} \mathcal{E}_c, \quad B^{(2)} = 0, \quad (20)$$

$$B^{(3)} = \frac{2g_B^4\sqrt{\kappa_{ex}}d_1}{\gamma(g_B^2 + d_1d_3)^2} \left(\frac{1}{d_1} + \frac{1}{d_1^*} \right) \left| \frac{\sqrt{\kappa_{ex}}d_1}{g_B^2 + d_1d_3} \right|^2 \mathcal{E}_c |\mathcal{E}_c|^2, \quad (21)$$

where $d_3 = i(\Delta_R - h) + \kappa_i/2 + \kappa_{ex}/2$. Correspondingly, the transmission field a_{out} and b_{out} can be explicitly expressed in the following form:

$$\begin{aligned} a_{\text{out}} &= -\mathcal{E}_c + \sqrt{\kappa_{ex}}B^{(1)} + \sqrt{\kappa_{ex}}B^{(3)} \\ &= \chi_a^{(1)}\mathcal{E}_c + \chi^{(3)}|\mathcal{E}_c|^2\mathcal{E}_c, \end{aligned} \quad (22)$$

$$\begin{aligned} b_{\text{out}} &= -\sqrt{\kappa_{ex}}B^{(1)} - \sqrt{\kappa_{ex}}B^{(3)} \\ &= -\chi_b^{(1)}\mathcal{E}_c - \chi^{(3)}|\mathcal{E}_c|^2\mathcal{E}_c, \end{aligned} \quad (23)$$

where $\chi_a^{(1)} = -1 + \frac{\kappa_{ex}d_1}{g_B^2 + d_1d_3}$, $\chi_b^{(1)} = \frac{\kappa_{ex}d_1}{g_B^2 + d_1d_3}$, and $\chi^{(3)} = \frac{2g_B^4\kappa_{ex}^2d_1}{\gamma(g_B^2 + d_1d_3)^2} \left(\frac{1}{d_1} + \frac{1}{d_1^*} \right) \left| \frac{d_1}{g_B^2 + d_1d_3} \right|^2$, respectively.

Case (iii) $kx = n\pi + \pi/4$. The atom couples simultaneously to two normal modes A and B . In this case, self-phase modulation (SPM) and cross-phase modulation (CPM) occur in the transmission fields a_{out} and b_{out} . Owing to the complicated function expression of optical nonlinearity with the high-order variable, we will adopt numerical simulations to demonstrate this effect in the following.

Before proceeding further, it is instructive to briefly analyze optical nonlinearities in our studied system, which is induced by the combination of the atom and the resonator with low-power optical input (a few nW). The power level of the driving laser is equal to several nW such that the third-order optical nonlinear effect of the dielectric high- Q resonator [such as the Kerr four-wave mixing (FWM) effect and stimulated Raman scattering [41]] and the saturation of the atom are absent in the proposed scheme. This atom-resonator-induced nonlinearity can be used to generate a type of optical frequency combs if driven with the bichromatic continuous-wave laser field in the following discussion. For the sake of convenience, here we assume the atom and resonator frequencies to be resonant, i.e., $\omega_A = \omega_R$ [24], so that the detuning $\Delta_A = \Delta_R = \Delta$. And we consider a monochromatic continuous-wave driving field, so the probe driving field is switched off ($\mathcal{E}_p = 0$). In all cases, the resonator is critically coupled ($\kappa_{ex} = \sqrt{\kappa_i^2 + h^2}$). Via numerical simulations, we display in Fig. 4 the magnitude of optical nonlinearities as a function of Δ for different x coordinates around the circumference of the toroid. From

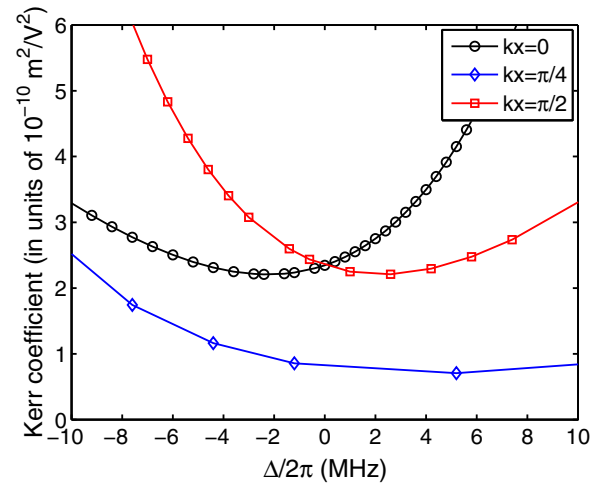


FIG. 4. (Color online) The Kerr nonlinearity $\chi^{(3)}$ (in units of m^2/V^2) as a function of relative detunings $\Delta_A = \Delta_R = \Delta$ (we consider the atom and cavity frequencies to be resonant) for different x coordinates around the circumference of the toroid, namely, (a) $kx = 0$, (b) $kx = \pi/4$, and (c) $kx = \pi/2$. In all cases, the resonator is critically coupled ($\kappa_{ex} = \sqrt{\kappa_i^2 + h^2}$) and the probe driving field is switched off ($\mathcal{E}_p = 0$). The system parameters for the simulation are chosen as atom-resonator interaction strength $g_0/2\pi = 70$ MHz, field decay rates for resonator modes $\kappa_i/2\pi = 75$ MHz, $\kappa_{ex}/2\pi = 90$ MHz, scattering strength $h/2\pi = 50$ MHz, and atomic spontaneous emission rate $\gamma/2\pi = 5.2$ MHz, respectively.

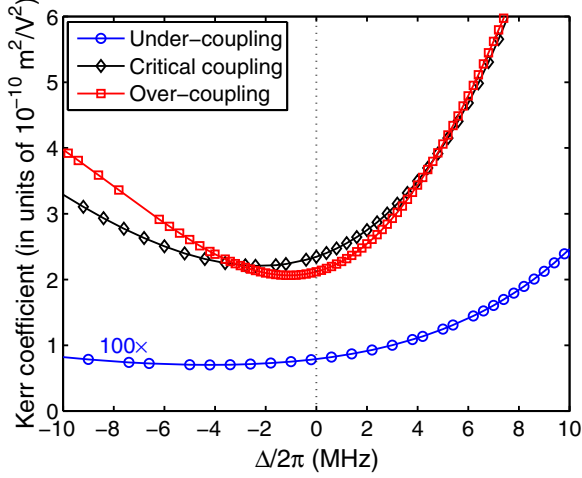


FIG. 5. (Color online) The Kerr nonlinearity $\chi^{(3)}$ (in units of m^2/V^2) as a function of relative detunings $\Delta_A = \Delta_R = \Delta$ for three different taper-resonator coupling regimes, namely, (a) undercoupling $\{\kappa_{ex}, \kappa_i, h\}/2\pi = \{5, 75, 50\}$ MHz, (b) critical coupling $\{\kappa_{ex}, \kappa_i, h\}/2\pi = \{90, 75, 50\}$ MHz, and (c) overcoupling $\{\kappa_{ex}, \kappa_i, h\}/2\pi = \{300, 75, 50\}$ MHz. In all cases, the probe driving field is switched off ($\mathcal{E}_p = 0$). The other system parameters are the same as Fig. 4 except for the azimuthal position of the atom $kx = 0$.

our calculation data of Fig. 4 at low values of control laser power, we infer $\chi^{(3)}(\Delta = 0) \approx 2.3 \times 10^{-10} \text{ m}^2/\text{V}^2$ at atomic localization with the well-defined azimuthal phase $kx = 0, \pi/2$ and $\chi^{(3)}(\Delta = 0) \approx 0.8 \times 10^{-10} \text{ m}^2/\text{V}^2$ at $kx = \pi/4$. These values are many orders of magnitude larger than the third-order optical nonlinear effect of the dielectric high- Q resonator with very high pump power [40,41].

In Fig. 5, we calculate the magnitude of optical nonlinearities as a function of Δ for different resonator coupling regimes. It is found from Fig. 5 that $\chi^{(3)}(\Delta = 0) \approx 7.9 \times 10^{-13} \text{ m}^2/\text{V}^2$ for undercoupling, $2.3 \times 10^{-10} \text{ m}^2/\text{V}^2$ for critical coupling, and $2.1 \times 10^{-10} \text{ m}^2/\text{V}^2$ for overcoupling. Note that when the interaction of the atom with the evanescent traveling-wave fields of the \hat{a}, \hat{b} modes is zero ($g_{tw} = 0$), we have the result $\chi^{(3)} = 0$. In the basis of the discussion above, we can reach the conclusion that the coherent coupling of the atom and the resonator induces a strong nonlinearity which is significantly stronger than Kerr nonlinearity in a microresonator made from a third-order nonlinearity material with high-power optical input (a few hundred mW). When two continuous-wave lasers in the tapered fiber are applied to drive the resonator mode and the power builds up in the resonator, this atom-resonator-induced nonlinearity gives rise to degenerate FWM via the interaction of the probe field \mathcal{E}_p with the control field \mathcal{E}_c [69,70]. The process of parametric FWM can yield a high conversion efficiency compared to Kerr FWM [40,41].

B. Optical-frequency-comb generation

Now we turn to discuss the frequency comb spectra of this coupled atom-resonator-fiber system when a bichromatic continuous-wave laser field [71] is guided by the fiber waveguide to only drive the resonator mode \hat{a} . The numerically simulated frequency comb spectra from the output of the driven

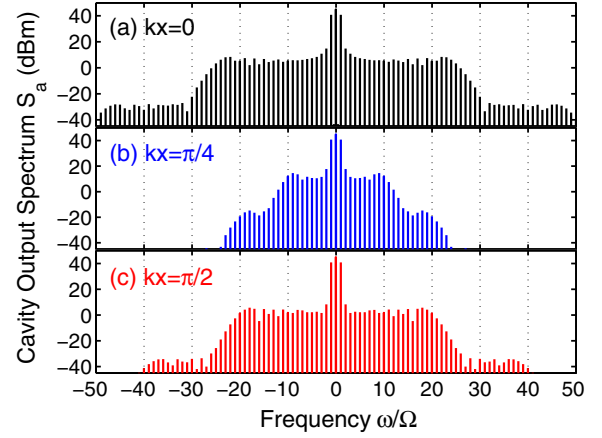


FIG. 6. (Color online) Generated frequency comb spectra from the resonator mode \hat{a} for three different x coordinates around the circumference of the toroid, namely, (a) $kx = 0$, (b) $kx = \pi/4$, and (c) $kx = \pi/2$. In all cases, the resonator is critically coupled ($\kappa_{ex} = \sqrt{\kappa_i^2 + h^2}$). Initially we assume that the atom is in its ground state $|g\rangle$. The other system parameters used for the simulations follow: atom-resonator interaction strength $g_0/2\pi = 70$ MHz, field decay rates for resonator modes $\kappa_i/2\pi = 75$ MHz, $\kappa_{ex}/2\pi = 90$ MHz, scattering strength $h/2\pi = 50$ MHz, driving laser strengths $\mathcal{E}_c = \mathcal{E}_p = 100 \text{ MHz}^{1/2}$ ($P_c = P_p = 84 \text{ nW}$), relative detunings $\Delta_A/2\pi = \Delta_R/2\pi = 0$, $\Omega/2\pi = 50$ MHz, and atomic spontaneous emission rate $\gamma/2\pi = 5.2$ MHz, respectively.

resonator mode \hat{a} as a function of ω/Ω are shown in Fig. 6 for three different x coordinates around the circumference of the toroid. For the case of atomic interaction with a single normal mode \hat{A} , such as azimuthal position $kx = 0$ in Fig. 6(a), a broad comb plateau is formed in the transmitted frequency spectra (pump line + generated sidebands), where all the comb lines have almost the same strength. Immediately after the plateau, the strengths of the high-order comb lines decrease rapidly. Whereas when $kx = \pi/4$ corresponding to atomic interaction with two normal modes \hat{A} and \hat{B} in Fig. 6(b), the number of the high-order comb lines is less than those in Fig. 6(a). This is because the parametric FWM process is weakened, resulting in inefficient sideband generation due to the weak nonlinearities $\chi^{(3)}$ for $kx = \pi/4$ as can be clearly seen from Fig. 4. For the case of atomic interaction with a single normal mode \hat{B} , such as $kx = \pi/2$ in Fig. 6(c), the strengths of the first few order comb lines in the transmitted frequency spectra decrease rapidly, followed by a broad plateau where all the sidebands have almost the same strength, and end up with a sharp cutoff. Such a typical ‘‘plateau-cutoff’’ spectral structure in Fig. 6 indicates that a new effect appears, which is reminiscent of high-order harmonic generation in intense laser-driven atoms system [72]. For this reason, we refer to this effect as an optical frequency microcomb generation in a whispering-gallery-mode microtoroid resonator. Figure 7 shows frequency comb spectra from the output of the resonator mode \hat{b} as a function of ω/Ω for three different x coordinates around the circumference of the toroid. The properties of the simulated optical frequency comb spectra are similar to those in Fig. 6. This is because the Hamiltonian of the system (1) is of the form of the linear exchange type coupling between the

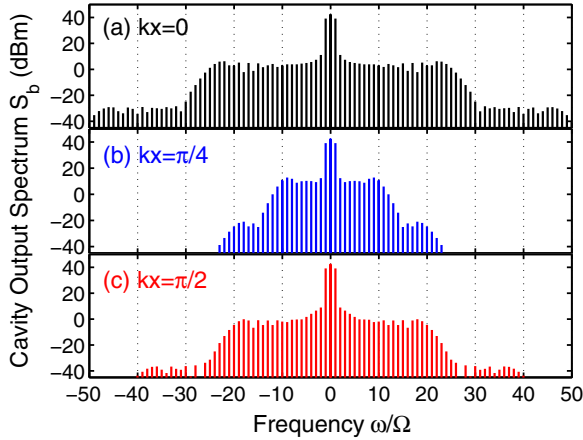


FIG. 7. (Color online) Generated frequency comb spectra from the resonator mode \hat{b} for three different x coordinates around the circumference of the toroid, namely, (a) $kx = 0$, (b) $kx = \pi/4$, and (c) $kx = \pi/2$. In all cases, the resonator is critically coupled ($\kappa_{ex} = \sqrt{\kappa_i^2 + h^2}$). The other system parameters are the same as Fig. 6.

cavity modes \hat{a} and \hat{b} , i.e., the term $h(\hat{a}\hat{b}^\dagger + \hat{a}^\dagger\hat{b})$. Therefore, an excitation present in the cavity mode \hat{a} can be coherently transferred through this exchange type coupling to the cavity mode \hat{b} . The transferred amount of energy is determined by the value of h .

An important aspect of the present atom-resonator-fiber QED system, associated with the input-output coupling efficiency of photons, is the ability to adjust the external coupling rate κ_{ex} of the resonator modes to the tapered fiber by tuning the distance between the WGM microtoroid resonator and the tapered fiber. Depending on the value of κ_{ex} relative to other coupling parameters, the microtoroid resonator QED system can exhibit quite distinct regimes of operation with regards to effect on a light field propagating along an evanescently coupled optical fiber. In order to further demonstrate the influence of the resonator coupling regimes, i.e., (i) undercoupling, (ii) critical coupling, and (iii) overcoupling, on the generated optical frequency-comb intensity, Figures 8 and 9 display the features of frequency comb spectra from the two resonator modes \hat{a} and \hat{b} , respectively. For the case of undercoupling $\{\kappa_{ex}, \kappa_i, h\}/2\pi = \{5, 75, 50\}$ MHz in Figs. 8(a) and 9(a), a few comb lines can be generated, however, their strengths are weak in the transmission spectra. The initial sidebands remain evident as strong peaks. Few four spectral lines with almost the same strength can be obtained as shown in Fig. 8(a). For the case of critical coupling $\{\kappa_{ex}, \kappa_i, h\}/2\pi = \{90, 75, 50\}$ MHz in Figs. 8(b) and 9(b), the comb shape is very different with respect to Figs. 8(a) and 9(a). Subsequent comb lines fill up the spectrum. A wide comb with a plateau can be achieved. The comb lines grow considerably and their peaks become more pronounced. For the case of overcoupling $\{\kappa_{ex}, \kappa_i, h\}/2\pi = \{300, 75, 50\}$ MHz in Figs. 8(c) and 9(c), the comb behavior is similar to those in Figs. 8(b) and 9(b) because their strong nonlinearities $\chi^{(3)}$ are close. Specifically, a comb plateau is formed, where all the sidebands have nearly the same strength, and then the comb spectra end up with a sharp cutoff. Physically, the shape of the comb can be explained by optical nonlinearity mentioned above. The atom-resonator-induced

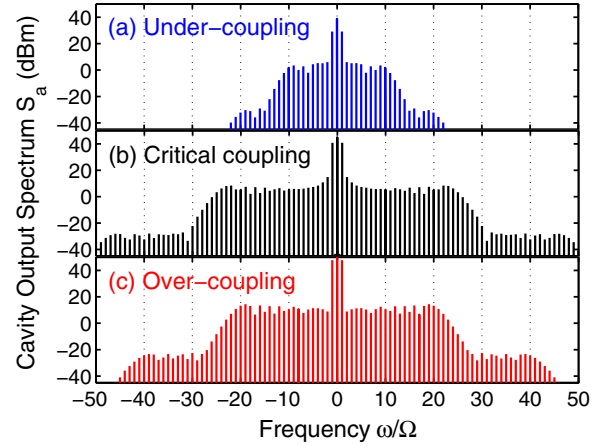


FIG. 8. (Color online) Generated frequency comb spectra from the resonator mode \hat{a} for three different resonator coupling regimes, namely, (a) undercoupling $\{\kappa_{ex}, \kappa_i, h\}/2\pi = \{5, 75, 50\}$ MHz, (b) critical coupling $\{\kappa_{ex}, \kappa_i, h\}/2\pi = \{90, 75, 50\}$ MHz, and (c) overcoupling $\{\kappa_{ex}, \kappa_i, h\}/2\pi = \{300, 75, 50\}$ MHz. The other system parameters are the same as Fig. 6 except for azimuthal position of the atom $kx = 0$.

nonlinearity is sufficiently large in Fig. 5 to cause efficient sideband generation through the parametric FWM process which results in the growth of the number of comb lines and the large spectral broadening of the combs.

Figure 10 shows the output comb spectra of the resonator mode \hat{a} for three different values of the relative detuning Ω between the control and probe laser frequencies. For the case that $\Omega/2\pi = 50$ MHz in Fig. 10(a), the comb consists of 95 lines with $2\pi \times 50$ MHz line spacing whose intensity beat can be directly measured using a fast photodiode. Whereas when $\Omega/2\pi = 100$ MHz in Fig. 10(b), the comb consists of 47 lines with a spacing of $2\pi \times 100$ MHz. With the further increase of

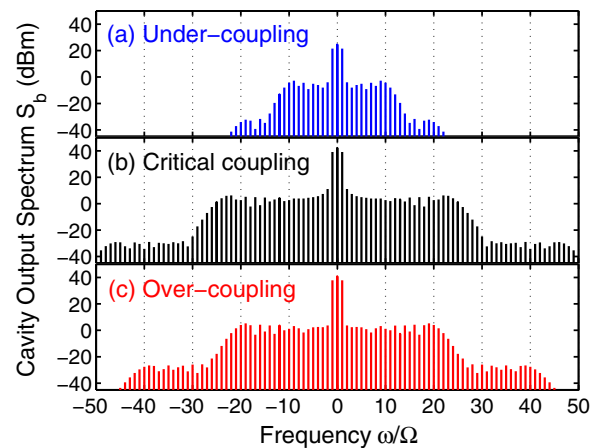


FIG. 9. (Color online) Generated frequency comb spectra from the resonator mode \hat{b} for three different resonator coupling regimes, namely, (a) undercoupling $\{\kappa_{ex}, \kappa_i, h\}/2\pi = \{5, 75, 50\}$ MHz, (b) critical coupling $\{\kappa_{ex}, \kappa_i, h\}/2\pi = \{90, 75, 50\}$ MHz, and (c) overcoupling $\{\kappa_{ex}, \kappa_i, h\}/2\pi = \{300, 75, 50\}$ MHz. The other system parameters are the same as Fig. 6 except for the azimuthal position of the atom $kx = 0$.

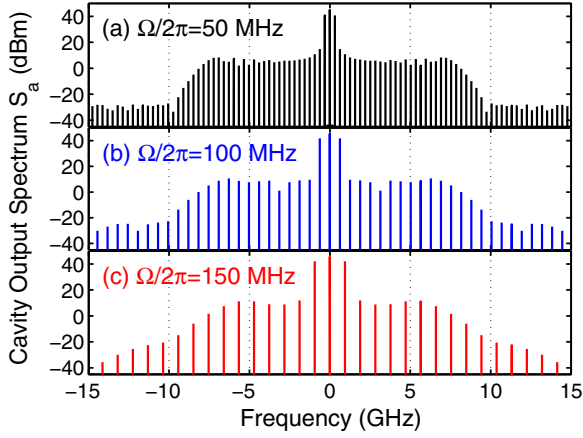


FIG. 10. (Color online) Generated frequency comb spectra from the resonator mode \hat{a} for three different values of the relative detuning Ω between the control and probe laser frequencies, namely, (a) $\Omega/2\pi = 50$ MHz, (b) $\Omega/2\pi = 100$ MHz, and (c) $\Omega/2\pi = 150$ MHz. In all cases, the resonator is critically coupled ($\kappa_{ex} = \sqrt{\kappa_i^2 + h^2}$). The other system parameters are the same as Fig. 6 except for the azimuthal position of the atom $kx = 0$.

Ω to a higher value such that $\Omega/2\pi = 150$ MHz as shown in Fig. 10(c), the frequency comb consists of 31 lines with $2\pi \times 150$ MHz line spacing. To sum up the above discussion, it is noticed that by simply varying the relative detuning Ω between the control and probe laser frequencies (the frequency beating $\Omega = \omega_c - \omega_p$), the frequency comb with different frequency spacings can be obtained in our device.

In what follows, we provide further the explicit explanations of the mode spacing of the optical frequency comb and the width of the comb line in Fig. 10. To this end, we will turn our attention to make the ansatz [68,73] for the above Heisenberg-Langevin equations to better understand the comb-generation behavior. Equations (3)–(7) in Sec. II are a set of nonlinear coupled equations and the optical response in the frequency domain is composed of many frequency components. In what follows we assume that the operators have been reduced to their expectation values. Since A , B , σ_{eg} , σ_{gg} , and σ_{ee} are periodic in frequency beating Ω , they can be expressed in the Fourier series as $A = \sum_n e^{-in\Omega t} A_n$, $B = \sum_n e^{-in\Omega t} B_n$, $\sigma_{eg} = \sum_n e^{-in\Omega t} \sigma_{eg,n}$, $\sigma_{gg} = \sum_n e^{-in\Omega t} \sigma_{gg,n}$, and $\sigma_{ee} = \sum_n e^{-in\Omega t} \sigma_{ee,n}$, respectively. In the notation $\sum_n = \sum_{n=-\infty}^{+\infty}$ the sum runs from negative infinity to positive infinity. After substituting the above Fourier series into Eqs. (3)–(7), we can obtain a series of coupled equations about A_n , B_n , $\sigma_{eg,n}$, $\sigma_{gg,n}$, and $\sigma_{ee,n}$ ($n = 0, \pm 1, \pm 2, \dots$) by resorting the prefactors in terms of the exponentials $e^{\pm in\Omega t}$. It is difficult to achieve the analytical solutions of these coupled equations and hence one has to resort to numerical solutions of them when all the higher-order moments (nonlinear terms) mentioned above are included. To obtain this task, the output fields from both resonator modes can be formally expressed in the time domain by $S_{out,a}(t) = \sqrt{\kappa_{ex}}\alpha_0 e^{-i\omega_c t} + \sqrt{\kappa_{ex}}\alpha_{+1} e^{-i(\omega_c + \Omega)t} + \sqrt{\kappa_{ex}}\alpha_{-1} e^{-i(\omega_c - \Omega)t} + \sqrt{\kappa_{ex}}\alpha_{+2} e^{-i(\omega_c + 2\Omega)t} + \sqrt{\kappa_{ex}}\alpha_{-2} e^{-i(\omega_c - 2\Omega)t} + \sqrt{\kappa_a}\alpha_{+3} e^{-i(\omega_c + 3\Omega)t} + \sqrt{\kappa_{ex}}\alpha_{-3} e^{-i(\omega_c - 3\Omega)t} + \dots$ and $S_{out,b}(t) = \sqrt{\kappa_{ex}}\beta_0 e^{-i\omega_c t} + \sqrt{\kappa_{ex}}\beta_{+1} e^{-i(\omega_c + \Omega)t} + \sqrt{\kappa_{ex}}\beta_{-1} e^{-i(\omega_c - \Omega)t} +$

$\sqrt{\kappa_{ex}}\beta_{+2} e^{-i(\omega_c + 2\Omega)t} + \sqrt{\kappa_{ex}}\beta_{-2} e^{-i(\omega_c - 2\Omega)t} + \sqrt{\kappa_b}\beta_{+3} e^{-i(\omega_c + 3\Omega)t} + \sqrt{\kappa_{ex}}\beta_{-3} e^{-i(\omega_c - 3\Omega)t} + \dots$, where $\alpha_0, \alpha_{+1}, \alpha_{-1}, \dots$ ($\beta_0, \beta_{+1}, \beta_{-1}, \dots$) are the corresponding transmission coefficients of the comb lines from the output fields of resonator mode \hat{a} (\hat{b}). It is easy to see from these expressions that the output fields contain two input components (the control field ω_c and the probe field ω_p) and a series of new components through the nonlinear optical process of parametric frequency conversion at frequencies $\omega_c - \Omega$ ($\equiv 2\omega_c - \omega_p$, the Stokes process), $\omega_c + 2\Omega$ ($\equiv 2\omega_p - \omega_c$, the second-order upper sideband process), $\omega_c - 2\Omega$ ($\equiv 3\omega_c - 2\omega_p$, the second-order lower sideband process), etc. As a consequence, when the atom-resonator system is driven by the bichromatic laser, i.e., the control field with frequency ω_c and the probe field with frequency ω_p , the parametric frequency conversion through nonlinear FWM appears [69], resulting in efficient sideband generation with frequencies $\omega_n = \omega_c + n \cdot \Omega$, where n is the number of the comb mode. That is to say, when the power builds up in the resonator, new frequency components are generated and interact by nonlinear FWM caused by the atom-resonator-induced strong nonlinearity. Obviously, the frequency spacing of the comb line is the difference Ω in the frequencies of the control and probe fields as can be verified in Fig. 10.

In addition, it is worth emphasizing that the generated frequency comb shown in Fig. 10 clearly exhibits a series of sharp lines even if zooming up the frequency axis, which can be well explained by the uncertainty relations of time and frequency. According to the uncertainty relations of time and frequency, it is straightforward to calculate the uncertainty of the frequency as $\Delta\omega \sim 2\pi/\Delta t$. Here, the applied driving laser is two continuous-wave lasers and it lasts about infinity, hence $\Delta t \rightarrow +\infty$. Immediately, we can arrive at the width of the observed comb lines $\Delta\omega \rightarrow 0$ in the frequency domain as shown in Fig. 10. As a result, the comb lines are relatively narrow sharp lines. Finally, we would like to point out that the transmission spectral width of the frequency combs in Figs. 6–9 depends on the numbers of the generated higher-order comb lines in the resonator output, which is determined by the atom-resonator-induced nonlinearity $\chi^{(3)}$. The optical nonlinearity $\chi^{(3)}$ is sufficiently large to cause efficient sideband generation through the parametric FWM process which results in the growth of the number of the comb lines and further the large spectral broadening of the frequency combs.

Before ending this section, we give a brief comment on more technical aspects regarding this model. First, a typical frequency separation between two adjacent modes of a microtoroidal resonator, i.e., the free spectral range (FSR) of the resonator, is larger than ~ 10 GHz [74], which is sufficiently larger than the resonator-enhanced decay rate of the atom considered here, i.e., $\Gamma = 4g_0^2/\kappa = 2\pi \times 119$ MHz. As a result, the coupling to other resonator modes is negligible. Second, the spectral width of the generated optical frequency combs is larger than ~ 14 GHz in our study, which is comparable to the FSR of the resonator. When the comb becomes broad, it is possible that the comb sidebands start to interact with other WGMs supported by the resonator. However, this coupling is very weak because it is the higher-order effect compared with the nonlinear effect of the system considered here. Therefore, the influence from the interaction of the comb

sidebands with other WGMs can be neglected. Finally, we have neglected the losses in the tapered fiber, assuming typical experimental setups.

IV. CONCLUSIONS

In summary, we have demonstrated a method to achieve fiber-optical frequency comb using a single atom coupled to a WGM microtoroidal resonator in low-power optical input. We systematically discuss and analyze the influences of different atomic azimuthal positions and taper-resonator coupling regimes on optical-frequency-comb generation. The results clearly show that the combination of the atom and the resonator can induce a large third-order nonlinearity which leads to a significant reduction in the threshold of nonlinear optical processes. This nonlinearity is significantly stronger than Kerr nonlinearity in previous implementations of Kerr frequency combs [41,43,44], which can be used to efficiently generate a frequency comb if driven coherently with two

continuous-wave lasers. The comb spacing is given by the frequency beating between the driving control and probe lasers. The atom-resonator-fiber QED scheme proposed here may find applications in a wide range of topics that include precision spectroscopy, atomic clocks, ultracold gases, and molecular fingerprinting.

ACKNOWLEDGMENTS

The authors express their gratitude to the anonymous referee of the paper for fruitful advice and comment, which significantly improved the paper. J.L. gratefully acknowledges Dr. Xiaoxue Yang for useful advice and discussion in manuscript preparation. This research was supported in part by the National Natural Science Foundation (NNSF) of China (Grants No. 11375067, No. 11404250, and No. 11275074), and the National Basic Research Program of China (Contract No. 2012CB922103).

-
- [1] K. J. Vahala, *Nature (London)* **424**, 839 (2003).
 [2] A. M. Armani, R. P. Kulkarni, S. E. Fraser, R. C. Flagan, and K. J. Vahala, *Science* **317**, 783 (2007).
 [3] J. Zhu, S. K. Ozdemir, Y. F. Xiao, L. Li, L. He, D. R. Chen, and L. Yang, *Nature Photon.* **4**, 46 (2010).
 [4] H. Mabuchi and A. C. Doherty, *Science* **298**, 1372 (2002).
 [5] S. M. Spillane, T. J. Kippenberg, K. J. Vahala, K. W. Goh, E. Wilcut, and H. J. Kimble, *Phys. Rev. A* **71**, 013817 (2005).
 [6] K. Hennessy, A. Badolato, M. Winger, D. Gerace, M. Atatüre, S. Gulde, S. Fält, E. L. Hu, and A. Imamoglu, *Nature (London)* **445**, 896 (2007).
 [7] H. J. Kimble, *Nature (London)* **453**, 1023 (2008).
 [8] M. Aspelmeyer, T. J. Kippenberg, and F. Marquardt, *arXiv:1303.0733*.
 [9] A. Schliesser and T. J. Kippenberg, *Adv. At. Mol. Opt. Phys.* **58**, 207 (2010).
 [10] G. Bahl, M. Tomes, F. Marquardt, and T. Carmon, *Nat. Phys.* **8**, 203 (2012).
 [11] S. M. Spillane, T. J. Kippenberg, and K. J. Vahala, *Nature (London)* **415**, 621 (2002).
 [12] J. Ward and O. Benson, *Laser Photonics Rev.* **5**, 553 (2011).
 [13] L. He, S. K. Ozdemir, J. Zhu, W. Kim, and L. Yang, *Nat. Nanotechnol.* **6**, 428 (2011).
 [14] Y. Wu and P. T. Leung, *Phys. Rev. A* **60**, 630 (1999).
 [15] V. S. Ilchenko and A. B. Matsko, *IEEE J. Sel. Top. Quantum Electron.* **12**, 15 (2006).
 [16] A. Chiasera, Y. Dumeige, P. Féron, M. Ferrari, Y. Jestin, G. N. Conti, S. Pelli, S. Soria, and G. C. Righini, *Laser Photonics Rev.* **4**, 457 (2010).
 [17] Y. Wu, X. Yang, and P. T. Leung, *Opt. Lett.* **24**, 345 (1999).
 [18] Y. Wu, *Phys. Rev. A* **61**, 033803 (2000).
 [19] S. M. Spillane, Ph.D thesis, California Institute of Technology, 2004.
 [20] X. Yi, Y. F. Xiao, Y. C. Liu, B. B. Li, Y. L. Chen, Y. Li, and Q. Gong, *Phys. Rev. A* **83**, 023803 (2011).
 [21] K. Srinivasan and O. Painter, *Phys. Rev. A* **75**, 023814 (2007).
 [22] S. M. Spillane, T. J. Kippenberg, O. J. Painter, and K. J. Vahala, *Phys. Rev. Lett.* **91**, 043902 (2003).
 [23] M. Cai, O. Painter, and K. J. Vahala, *Phys. Rev. Lett.* **85**, 74 (2000).
 [24] B. Dayan, A. S. Parkins, T. Aoki, H. J. Kimble, E. P. Ostby, and K. J. Vahala, *Science* **319**, 1062 (2008).
 [25] Y. C. Liu, Y. F. Xiao, B. B. Li, X. F. Jiang, Y. Li, and Q. Gong, *Phys. Rev. A* **84**, 011805(R) (2011).
 [26] T. Aoki, A. S. Parkins, D. J. Alton, C. A. Regal, B. Dayan, E. Ostby, K. J. Vahala, and H. J. Kimble, *Phys. Rev. Lett.* **102**, 083601 (2009).
 [27] I. Shomroni, S. Rosenblum, Y. Lovsky, O. Bechler, G. Guendelman, and B. Dayan, *arXiv:1405.0937*.
 [28] F. Y. Hong and S. J. Xiong, *Phys. Rev. A* **78**, 013812 (2008).
 [29] D. O'Shea, C. Junge, J. Volz, and A. Rauschenbeutel, *Phys. Rev. Lett.* **111**, 193601 (2013).
 [30] S. Parkins and T. Aoki, *arXiv:1405.6776*.
 [31] Y. F. Xiao, Z. F. Han, and G. C. Guo, *Phys. Rev. A* **73**, 052324 (2006).
 [32] J. S. Jin, C. S. Yu, P. Pei, and H. S. Song, *Phys. Rev. A* **81**, 042309 (2010).
 [33] T. Aoki, B. Dayan, E. Wilcut, W. P. Bowen, A. S. Parkins, T. J. Kippenberg, K. J. Vahala, and H. J. Kimble, *Nature (London)* **443**, 671 (2006).
 [34] D. J. Alton, N. P. Stern, T. Aoki, H. Lee, E. Ostby, K. J. Vahala, and H. J. Kimble, *Nat. Phys.* **7**, 159 (2010).
 [35] C. Junge, D. O'Shea, J. Volz, and A. Rauschenbeutel, *Phys. Rev. Lett.* **110**, 213604 (2013).
 [36] S. T. Cundiff and J. Ye, *Rev. Mod. Phys.* **75**, 325 (2003).
 [37] U. Keller, *Nature (London)* **424**, 831 (2003).
 [38] A. Schliesser, N. Picque, and T. W. Hänsch, *Nature Photon.* **6**, 440 (2012).
 [39] Th. Udem, R. Holzwarth, and T. W. Hänsch, *Nature (London)* **416**, 233 (2002).
 [40] P. Del'Haye, A. Schliesser, O. Arcizet, T. Wilken, R. Holzwarth, and T. J. Kippenberg, *Nature (London)* **450**, 1214 (2007).
 [41] T. J. Kippenberg, R. Holzwarth, and S. A. Diddams, *Science* **332**, 555 (2011).
 [42] A. A. Savchenkov, A. B. Matsko, V. S. Ilchenko, I. Solomatine, D. Seidel, and L. Maleki, *Phys. Rev. Lett.* **101**, 093902 (2008).

- [43] I. S. Grudin, N. Yu, and L. Maleki, *Opt. Lett.* **34**, 878 (2009).
- [44] T. Herr, K. Hartinger, J. Riemensberger, C. Y. Wang, E. Gavartin, R. Holzwarth, M. L. Gorodetsky, and T. J. Kippenberg, *Nature Photon.* **6**, 480 (2012).
- [45] P. Del'Haye, T. Herr, E. Gavartin, M. L. Gorodetsky, R. Holzwarth, and T. J. Kippenberg, *Phys. Rev. Lett.* **107**, 063901 (2011).
- [46] Y. K. Chembo, D. V. Strekalov, and N. Yu, *Phys. Rev. Lett.* **104**, 103902 (2010).
- [47] P. Del'Haye, O. Arcizet, A. Schliesser, R. Holzwarth, and T. J. Kippenberg, *Phys. Rev. Lett.* **101**, 053903 (2008).
- [48] W. Loh, P. Del'Haye, S. B. Papp, and S. A. Diddams, *Phys. Rev. A* **89**, 053810 (2014).
- [49] P. Del'Haye, K. Beha, S. B. Papp, and S. A. Diddams, *Phys. Rev. Lett.* **112**, 043905 (2014).
- [50] Supporting online material accompanying Ref. [24].
- [51] Supporting online material accompanying Ref. [33].
- [52] K. Xia and J. Twamley, *Phys. Rev. X* **3**, 031013 (2013).
- [53] M. Rosenblit, P. Horak, S. Hellsby, and R. Folman, *Phys. Rev. A* **70**, 053808 (2004).
- [54] K. Koshino and T. Aoki, *Phys. Rev. A* **89**, 023814 (2014).
- [55] J. T. Shen and S. Fan, *Phys. Rev. A* **82**, 021802(R) (2010).
- [56] S. I. Schmid and J. Evers, *Phys. Rev. A* **84**, 053822 (2011).
- [57] K. Srinivasan and O. Painter, *Nature (London)* **450**, 862 (2007).
- [58] I. Fushman, D. Englund, A. Faraon, N. Stoltz, P. Petroff, and J. Vučković, *Science* **320**, 769 (2008).
- [59] J. Li, R. Yu, C. Ding, W. Wang, and Y. Wu, *Phys. Rev. A* **90**, 033830 (2014).
- [60] Y. D. Kwon, M. A. Armen, and H. Mabuchi, *Phys. Rev. Lett.* **111**, 203002 (2013).
- [61] T. Carmon, M. C. Cross, and K. J. Vahala, *Phys. Rev. Lett.* **98**, 167203 (2007).
- [62] A. Majumdar, M. Bajcsy, D. Englund, and J. Vučković, *IEEE J. Sel. Top. Quantum Electron.* **18**, 1812 (2012).
- [63] E. Waks and D. Sridharan, *Phys. Rev. A* **82**, 043845 (2010).
- [64] A. C. Newell and J. V. Moloney, *Nonlinear Optics* (Addison-Wesley, Redwood City, 1992).
- [65] E. Waks and J. Vuckovic, *Phys. Rev. Lett.* **96**, 153601 (2006).
- [66] S. Fan, Ş. E. Kocabaş, and J. T. Shen, *Phys. Rev. A* **82**, 063821 (2010).
- [67] E. Rephaeli and S. Fan, *IEEE J. Sel. Top. Quantum Electron.* **18**, 1754 (2012).
- [68] R. W. Boyd, *Nonlinear Optics* (Academic, San Diego, 2008).
- [69] R. W. Boyd, M. G. Raymer, P. Narum, and D. J. Harter, *Phys. Rev. A* **24**, 411 (1981); R. S. Bennink, R. W. Boyd, C. R. Stroud, Jr., and V. Wong, *ibid.* **63**, 033804 (2001).
- [70] Y. Zhang, C. Zuo, H. Zheng, C. Li, Z. Nie, J. Song, H. Chang, and M. Xiao, *Phys. Rev. A* **80**, 055804 (2009).
- [71] T. Hansson and S. Wabnitz, *Phys. Rev. A* **90**, 013811 (2014).
- [72] T. Brabec and F. Krausz, *Rev. Mod. Phys.* **72**, 545 (2000).
- [73] K. Y. Fong, M. Poot, X. Han, and H. X. Tang, *arXiv:1404.3434*.
- [74] J. Yao, D. Leuenberger, M. M. Lee, and M. C. Wu, *IEEE J. Sel. Top. Quantum Electron.* **13**, 202 (2007).